Article

Cobalt-/Copper-Containing Perovskites in Oxygen Evolution and Reduction Reactions

Taymaz Tabari,* Marcin Kobielusz, Dheerendra Singh, Jiaguo Yu, and Wojciech Macyk*

Cite This: ACS Appl. Eng. Mater. 2023, 1, 2207−2216

Read Online

ACCESS | Metrics & More | Article Recommendations | Supporting Information

ABSTRACT: The design and engineering of electrocatalysts for the oxygen reduction reaction (ORR) and oxygen evolution reaction (OER) are key to sustainable development. The structure of ABO_3 perovskites allows engineering of their electronic properties such as the energy of the Fermi level and the valence band maximum, which directly impact their electrocatalytic activity. Moreover, the covalency of the B−O bond and its electron affinity increase the polarization of −OH adsorbed at B-sites, leading to enhanced kinetics of OER. Here, a series of cobalt/copper perovskites ($Ca_{0.8}Sr_{0.2}Co_{1-x}Cu_xO_{3-\delta}$ ($x = 0$, 0.5, and 1)) were prepared. In our finding, copper with a larger electron affinity compared to cobalt accelerates OER, while the coexistence of Co/Cu at the B-sites increases the activity of the system in ORR. The mechanism of OER is discussed based on the pH dependency on the reversible hydrogen electrode (RHE) scale and galvanostatic oxidation measurements. The results point to the lattice oxygen mechanism as the prevailing one.

KEYWORDS: catalyst design, water splitting, electrocatalysis, cobalt/copper perovskite, engineering of redox properties
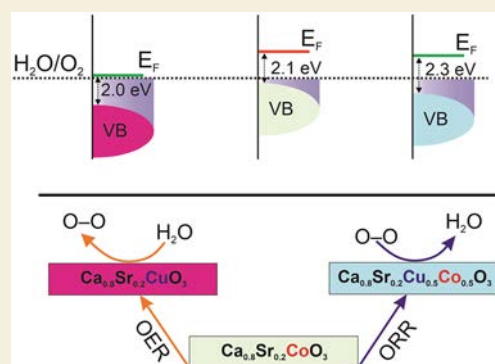
1. INTRODUCTION

Sustainable energy conversion and storage are at the center of attention due to limited fossil fuel resources.[1] Electrocatalytic water splitting,[2] rechargeable metal-air batteries, and proton-exchange membrane fuel cells are the future of green energy production.[3] To split water into hydrogen and oxygen, 237 kJ mol^{-1} is needed. The half oxidation reaction, known as the oxygen evolution reaction (OER), occurs at the anode. Likewise, the oxygen reduction reaction, ORR, which takes place at the cathode, needs 498 kJ mol^{-1} to break the O=O bond.[4] During OER and ORR, strong adsorption of the reactants on the surface of the electrocatalyst is crucial for the high efficiencies of these processes.[5] The most active electrocatalysts for such reactions are precious metals and their oxides, which are costly.[6] Alternatively, copper oxide shows promising activity in the oxidation of water.[7] However, stability along with the size- and shape-dependent activity of this catalyst remains an issue for long-term applications.[8] The ABO_3 perovskites possess a high activity in OER and ORR, which allows using them in various technologies such as fuel cells, batteries, and electrocatalysis.[9] Perovskites' tunable structure empowers engineering of the thermodynamic properties, which control their overall efficiency in the targeted reactions. A few copper-based perovskites were developed and published recently, pointing at their phenomenal oxidative potential against organic dyes,[10] quinolone antibiotics,[11] and bisphenol A,[12] revealing their exceptional stability for long-term use. These publications mostly deal with the removal of

the organic compounds via catalytic routes, with less focus on the thermodynamic properties of the Cu-containing perovskites. Moreover, recent publications on cobalt-containing perovskites show that $SrCoO_3$ and $CaCoO_3$ possess a higher efficiency compared to $LaCoO_3$. In this context, the performance of cobalt-containing perovskites (e.g., $LaCoO_3$ and $SrCoO_3$) in OER was studied profoundly by employing density functional theory (DFT) calculations, focusing on their energetic properties, especially the energy of the Fermi level (E_F).[13,14] Shao-Horn et al. showed that the difference in the activity of perovskites stems from the position of Fermi levels in the $SrCoO_3$ perovskite, compared to $LaCoO_3$.[13,14] In other words, the increased proportion of Co^{4+} in $SrCoO_3$ leads to the shift of Fermi levels toward the O 2p orbitals, increasing the efficiency in OER. However, $SrCoO_3$ contains a large portion of Co^{3+} as well, which is due to the presence of oxygen vacancies.[13,15] Thus, following the development path of the cobalt-containing perovskites, to enhance the catalytic activity of ABO_3 perovskites, adding Cu^{2+} (with cobalt) to the B site, which is its stable formal oxidation number, will trigger the system to compensate for the lack of the charge, increasing the
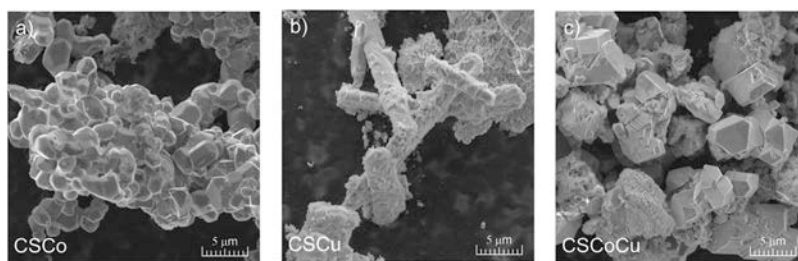
Figure 1. SEM images of the CSCo (a), CSCu (b), and CSCoCu (c) samples.

proportion of Co^{4+} to Co^{3+}. The perovskites will inherit the oxidative properties of copper as well. Furthermore, the presence of Ca in the A site along with Sr will increase the oxygen permeability of the perovskites, which will modify the activity of the B-sites.[16] Therefore, in this study, $Ca_{0.8}Sr_{0.2}Co_{1-x}Cu_xO_{3-\delta}$ (x = 0, 0.5, and 1) perovskites were synthesized using the sol−gel method; then, the electrocatalytic properties of the perovskites in OER were investigated concerning their thermodynamic properties such as Fermi levels and energy of the valence band (VB).

2. MATERIALS AND METHODS

2.1. Synthesis of $Ca_{0.8}Sr_{0.2}Co_{1-x}Cu_xO_{3-\delta}$ (x = 0, 0.5, and 1) Perovskites

The perovskites were synthesized using the sol−gel method. Herein, a stoichiometric amount of metal nitrates was dissolved in water under vigorous stirring. Then, citric acid as a ligand was added to the solution containing the metal nitrates, while the molar ratio of metals to ligand was 1:2. The solution was kept under stirring for the next hour at 80 °C to obtain a gel. Following, the gel was placed in an autoclave, which was adjusted at 120 °C to dry it. Then, it was ground and transferred as a powder to a muffle furnace and calcined at 850 °C for 4 h, while the increasing rate of the temperature was 10 °C min⁻¹. The characterization techniques and the condition to analyze the materials were similar to our previous publications (please check the Supporting Information (SI) section).[17]

2.2. Electrochemical Characterization of the Perovskites

The activity of the electrodes was tested in the oxygen reduction reaction (ORR) and the oxygen evolution reaction (OER). A rotating ring disk electrode (RRDE) was connected to the Autolab potentiostat/galvanostat (PGSTAT302N) in a three-electrode configuration, and the Pt and Ag/AgCl (3 M_{KCl}) were used as the counter and reference electrodes, respectively, while the working electrode was a glassy carbon coated with catalyst ink prepared using the drop-cast method.[15] 10 mg of perovskite powder was physically mixed with 2 mg of Super P carbon black (Alfa Aesar). Then, the obtained mixture was dispersed in a solution consisting of 100 μL of 5 wt % Nafion 117 (Sigma-Aldrich) and 900 μL of absolute ethanol. The suspension was sonicated for 2 h, and 5 μL of the obtained ink was used to place the catalyst on the glassy carbon electrode. To prevent any unwanted non-Faradic reactions at the surface of the electrode, it underwent 30 cycles of cyclic voltammetry (CV) between 0 and 1.2 V vs a reversible hydrogen electrode (RHE) at 0.01 V s⁻¹ scan rate. The linear sweep voltammetry (LSV) measurements were conducted in 0.1 M KOH (pH = 13) with a scan rate of 0.01 V s⁻¹, while the rotational speed was set from 800 to 2000 rpm (stepwise increased by 400 rpm). Furthermore, the OER activity tests were performed in 1 M KOH solution, while the applied potential was from 1.2 to 1.72 V vs RHE. The OER measurements were performed under 3000 rpm rotation speed using RRDE. The galvanostatic measurements were conducted in 1 M KOH and 200 μg cm⁻² load of the catalyst. The potential was converted to RHE using the Nernst equation $V_{RHE} = V_{applied\ potential}$ + 0.2 $V_{(Ag/AgCl)}$ + 0.059 pH. Electrochemical impedance spectroscopy (EIS) was conducted with a frequency range from 100 kHz to 0.1 Hz.

The Ag/AgCl electrode was calibrated in the same electrolyte by measuring the hydrogen oxidation/evolution at a Pt electrode, finding the 0 V vs RHE, reported by Shao-Horn et al.[14] The platinum electrode was cleaned before every measurement by applying 2 V vs Ag/AgCl for 2 min using 0.5 M H_2SO_4 as the electrolyte and then sonicated in water for 1 min. Notably, owing to the highly alkaline electrolytes, the Pt migration and deposition on the working electrode can be neglected.[18]

3. RESULTS AND DISCUSSION

3.1. Physicochemical Analysis

Figure S1 depicts the X-ray diffraction (XRD) patterns of the synthesized materials, $Ca_{0.8}Sr_{0.2}CoO_{3-\delta}$ (CSCo),[19] $Ca_{0.8}Sr_{0.2}CuO_{3-\delta}$ (CSCu),[10] and $Ca_{0.8}Sr_{0.2}Co_{0.5}Cu_{0.5}O_{3-\delta}$ (CSCoCu), confirming their perovskite structure. The XRD pattern shows peaks at 2θ of 23.0, 31.5, 39.5, 46.5, and 57.0°, which are related to the pure crystalline structure of CSCo (space group: $Pm\bar{3}m$), which is in good agreement with a previous report.[20] The Rietveld refinement indicated the presence of single-phase perovskite for CSCo. In the case of CSCu, the peaks at 2θ 25.3, 25.8, 28.9, 32.0, 35.3, 37.3, 38.5, 44.4, 48.7, and 53.8° are attributed to the perovskite's crystalline phase correlating with $Ca_{1.46}Sr_{2.38}Cu_4O_{8-\delta}$, while the presence of a secondary perovskite is also detected, depicting the presence of $Ca_{3.64}Sr_{0.36}Cu_2O_6$ as a secondary perovskite. CSCu shows an XRD pattern of infinite-layered perovskites. These perovskites have highly defective structures, in which one-third of the oxygen positions are vacant/empty, as previously shown by Chen et al.[21] In the crystal structure of $Ca_{1-x}Sr_xCuO_2$, both Sr^{2+} and Ca^{2+} ions separate the Cu_2O layers, and the partial concentration of Ca/Sr can be varied between the layers. The change in the ratio of Ca and Sr induces the crystallization of the perovskites in two different phases, both of which are perovskites. Rietveld analysis confirms the presence of these two perovskites, demonstrated in Figure S1. The parameters of the refinement are shown in Table S2a−c. The observed shift to the lower angles in CSCu compared to CSCo is related to the larger ionic radius of Cu^{2+} compared to both Co^{3+} and Co^{4+}. CSCoCu peaks at 2θ = 31.0, 32.2, 34.0, 37.5, and 43.2° reveal the crystal structure of the perovskite, and Rietveld analysis confirmed the presence of a single-phase perovskite, in which B-sites are occupied by Co and Cu. CSCoCu compared to CSCu and CSCo shows one major crystalline phase following the pattern of both CSCo and CSCu. However, a slight shift in the position of the peaks is observed, which can be attributed to the presence of Co and Cu with different atomic radii at the B site of CSCoCu. Table S1 shows data obtained from N_2-adsorption/desorption measurements.
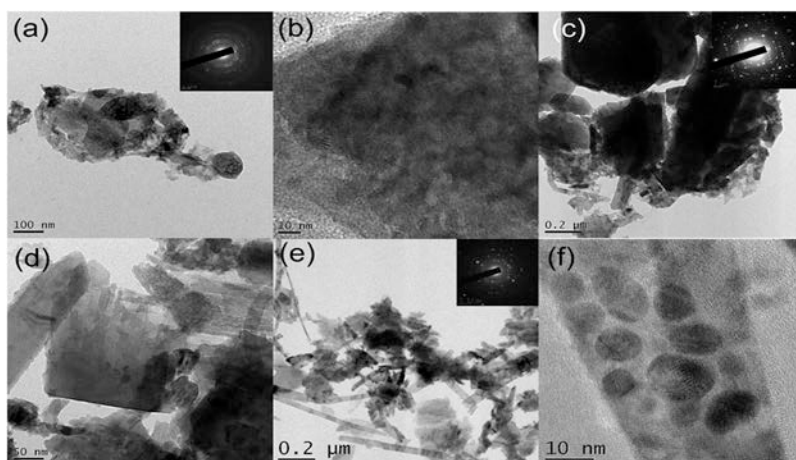
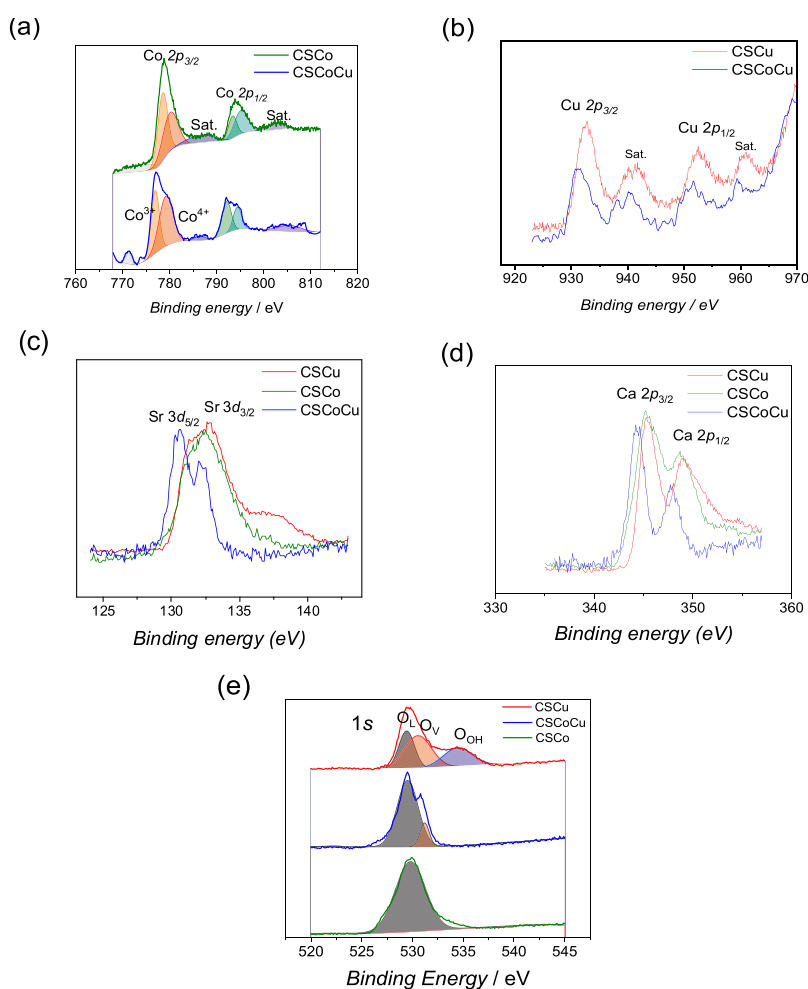**Figure 2.** TEM analysis: CSCo (a, b), CSCu (c, d), and CSCoCu (e, f).

Figure 3. XPS core-level analysis: Co 2p (a), Cu 2p (b), Sr 3d (c), Ca 2p (d), and O 1s (e). O_L, O_V, and O_{OH} stand for lattice, adsorbed water, and surface oxygen, respectively.

3.2. Morphology

The scanning electron microscopy (SEM) image shows that CSCo exists as agglomerated, uniform truncated hexagonal crystals (Figure 1a). Figure 1b shows two forms of CSCu, a well-grown rod structure covered by aggregated small particles. The rods are not uniform but are formed from smaller subunits. Figure 1c depicts large truncated hexagonal crystals

of CSCuCo with clear, sharp edges. The transmission electron microscopy (TEM) image of CSCo (Figure 2a) shows particles aggregated during the heating process. The closer view shown in Figure 2b reveals that every grain is composed of smaller particles. The rings in the selected area electron diffraction (SAED) pattern point at the crystalline structure of the CSCo. Figure 2c,d depicts CSCu in the form of irregular aggregates composed of elongated units, complying with the
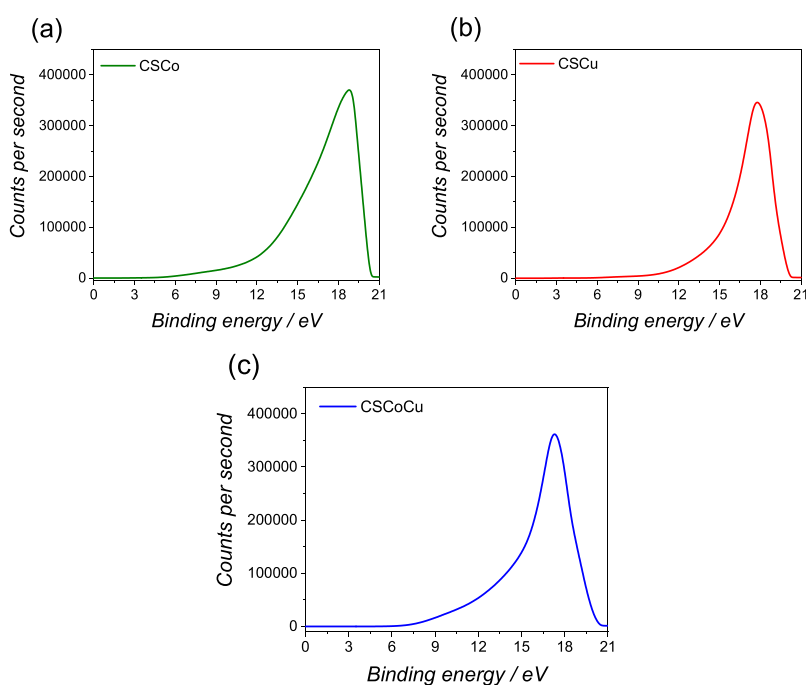
Figure 4. Ultraviolet photoelectron spectroscopy of CSCo (a), CSCu (b), and CSCoCu (c).

SEM image (Figure 1b). The TEM images of CSCoCu shown in Figure 2e,f reveal the straw structure of CSCoCu (of different thicknesses) mixed with less organized aggregates. The higher magnification (Figure 2f) also shows small particles attached to the straws. In addition to the straw architecture, large crystals of CSCoCu exist, as presented in the SEM image. The SAED confirms the polycrystalline structure of the material.

3.3. X-ray Photoelectron Spectroscopy (XPS)

The survey analysis of X-ray photoelectron spectroscopy (XPS) is shown in Figure S2, while the XPS core-level analysis is shown in Figure 3. The satellite peaks of cobalt in CSCo reveal the presence of Co^{3+}, while a small fraction of Co^{4+} coexists at the B-sites.[22,23] In CSCoCu, the Co^{4+}/Co^{3+} ratio increases dramatically, while the Co^{3+} satellite peak's intensity decreases compared to CSCo. The core-level analysis of Cu shows the Cu 2p peak of CSCoCu and CSCu, while the satellite peaks reveal the existence of copper in the +2 oxidation state. The oxygen core-level analysis of CSCu shows a larger content of surface oxygen compared to CSCoCu and CSCo. In other words, the cobalt core-level analysis (Figure 3a) indicates the presence of Co^{3+}, which is revealed by the satellite peaks of cobalt(III), while deconvoluting Co $2p_{1/2}$ and Co $2p_{3/2}$ peaks point to the presence of Co^{4+}. By adding Cu^{2+}, the ratio of Co^{4+}/Co^{3+} increased in CSCoCu compared to CSCo, which was expected, as the cobalt(IV) should compensate for the electric charge of the system. Moreover, the satellite peak of Cu^{2+} (Figure 3b) reveals the oxidation states of copper(II). In other words, in both CSCo and CSCoCu, copper is present as copper(II). The XPS core analysis of strontium (Figure 3c) can be divided into two regions specific to lattice and surface strontium. The lattice strontium region extends from 128 to 135 eV, while the surface strontium region appears between 130 and 140 eV.[24] The core analysis of Ca (Figure 3d) shows two peaks attributed to Ca $2p_{1/2}$ and Ca $2p_{3/2}$ at 348 and 343 eV, respectively. The spin-energy separation of these peaks is 3.2 eV, indicating the

presence of Ca^{2+} in the perovskite structure without its significant signal from an additional phase.[25] In addition, different electronic states of metals (Ca, Sr, Cu, and Co) influence the binding energy of oxygen. The deconvolution of the O 1s peak (Figure 3e) shows the presence of lattice oxygen atoms (525−530 eV) along with the chemisorbed oxygen (H_2O and OH group) that appears in the range of 530−540 eV.[26]

3.4. Energetic Properties

The valence band maxima (VBM) and Femi levels were calculated using the first and secondary edges of the spectra obtained employing ultraviolet photoelectron spectroscopy (UPS), discussed in our previous publication;[22] the UPS analysis provides a relative energy value versus the vacuum level. The calculated work functions (ϕ) for CSCo and CSCu (Figure 4) are 4.4 and 4.9 eV, respectively, while the VBM energies amount to −6.8 and −7.2 eV, respectively. The work function and VBM of CSCoCu are equal to 4.2 and −7.0 eV, respectively. The work function values obtained for CSCo and CSCoCu are slightly different, while CSCu shows a significant difference compared to the cobalt-containing perovskites. Moreover, the valence band maxima of the CSCoCu value are in between CSCo and CSCu. These results indicate that the electronic properties of CSCoCu have similarities to both pristine CSCo and CSCu perovskites.

The results of work function (ϕ) measurements with the Kelvin probe (KP) under vacuum and atmospheric conditions together with the obtained work function values from UPS are shown in Figure 5. The recorded values from both analyses, KP and UPS measurements, corroborate with each other. The energy of the Fermi level (E_F) of CSCoCu is higher compared to CSCo and CSCu. The XPS core analysis of Co 2p demonstrated an increase in the ratio of Co^{4+} to Co^{3+}. Previous reports on Co-containing perovskites suggest that increasing the content of Co^{4+} lowers the Fermi level (which can be interpreted as an increase in the work function). It is correct in theory since losing one electron from Co^{3+}, and turning it to
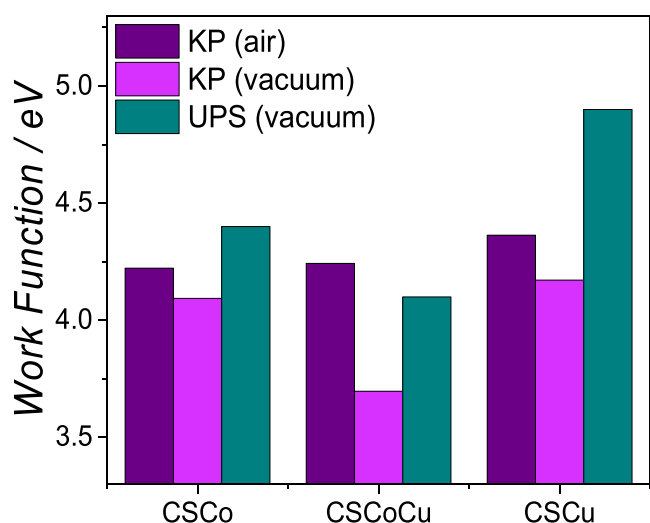
Figure 5. Work function values were measured by KP and UPS under ambient and vacuum conditions.

Co^{4+}, decreases the number of electrons and lowers the Fermi level. However, in this study, the results of both KP and UPS measurements show that the work function value decreases in the presence of the increased content of Co^{4+}, indicating the elevation of Fermi levels. Previously, we had shown that the increased oxidation states of iron induce Jahn−Teller distortion, which will alter the position of Fermi levels.[17] Nevertheless, one should be aware that the Jahn−Teller distortion is prominent when e_g orbitals are occupied in a nondegenerate way. In a low-spin Co^{4+}, the nondegenerate occupation is related to t_{2g} orbitals, which implies insignificant Jahn−Teller distortions. Therefore, the decreased work function values by increasing the content of Co^{4+} should not be related to the Jahn−Teller distortion. This upward shift of the Fermi levels was also reported by Zhu et al. in the case of $LaCoO_3$[27] and in our current report about $LaFeO_3$ perovskites.[28] These changes in the Fermi level of the perovskites can be different under vacuum and ambient conditions. The KP measurements under ambient conditions (Figure 5) indicate a significant increase in work function values. This phenomenon solely decreases the distance between the Fermi levels and the VBM of the perovskites, affecting their total activity in ORR and OER. Herein, the increased work function values, which can be interpreted as decreased Fermi levels, are evident from the O 1s core-level analysis. The increased content of Co^{4+} to Co^{3+} induces an increased adsorbed water and hydroxyl species, in which electron flows from the Fermi levels of the perovskites to the oxygen and hydroxyl species, evident from the KP results, and both can lower the Fermi level, increasing the work functions. Under the vacuum, CSCoCu indicated a higher Fermi level compared to CSCu and CSCo; however, the adsorbed water and OH groups dramatically decreased the position of Fermi levels—this phenomenon was reported by Kim et al., as well.[29] Moreover, under ambient conditions, the highest ϕ shift (+0.5 eV) is observed for CSCoCu, as electrons from E_F of CSCoCu can be transferred to the adsorbates such as oxygen molecules (Figure 2c). This shift lowers the Fermi levels toward the VBM.

The density of electronic states (DOS) at the top of the valence band (VB) (Figure 4) shows a significant change in the density and distribution of these states of CSCoCu compared to CSCo and CSCu. The DOS shape of CSCoCu

demonstrates features of both CSCo and CSCu. Varignon et al. have shown that the VB of ABO_3 perovskites is mostly constructed of O 2p orbitals,[30] which interact with d-orbitals of B-sites, determining the Fermi levels.[14,31] The UPS successfully demonstrates the energy difference (E_{diff}) between VBM and E_F, which can directly be translated to the energy difference between the top of O 2p orbitals (valence orbital level) and the Fermi levels. This difference correlates with the difference between the Fermi levels and the O 2p center, previously shown by Shao-Horn et al.[14] Therefore, employing UPS, and KP results, the electronic configuration of the perovskite can be illustrated under vacuum and ambient conditions, shown in Figure 6.
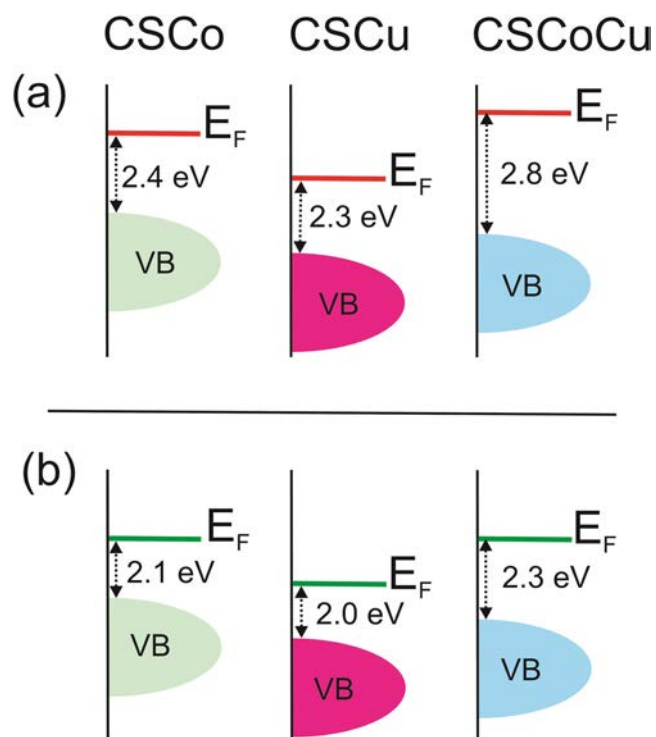

Figure 6. Energetic diagrams of perovskites: under vacuum (a) and ambient (b) conditions.

3.5. Electrocatalytic Activity

3.5.1. Oxygen Reduction Reaction. The oxygen reduction peak, depicted in CV (Figure S3a,b), remains unchanged even after 30 cycles for CSCoCu, while its decrease is evident in the cases of CSCo and CSCu. The LSV measurements (Figures 7a and S3c−e) revealed the ORR onset potentials increasing on the order of CSCu, CSCo, and CSCoCu (0.68, 0.71, and 0.77 V *vs* RHE, respectively), indicating the advantage of CSCoCu compared to CSCo and CSCu. The half-wave potentials of ORR for CSCu, CSCo, and CSCoCu are 0.537, 0.567, and 0.597 V *vs* RHE, while the diffusion-limited currents are 1.51, 2.37, and 3.38 mA cm^{-2}, respectively, pointing at the enhanced activity of CSCoCu. The Koutecky−Levich (K−L) plots were employed to calculate the number of electrons exchanged between the catalyst and the reactant (Figure S3f−h). The plots reveal the first-order mechanism involving $4e^-$ in ORR within 0.03−1.2 V *vs* RHE. CSCoCu with 3.82 electrons showed the highest activity, while CSCo and CSCu indicated a transfer of 3.75 and 3.25 electrons, respectively. The four-electron transfer, typical for
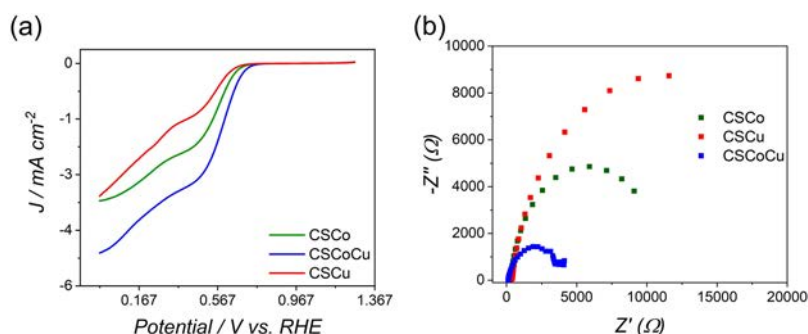
Figure 7. Linear sweep voltammetry measurement with RRDE in an oxygen-saturated solution (2000 rpm) (a) and the EIS measurements (ORR; frequency range from 100 kHz to 0.1 Hz; applied potential of 0.5 V *vs* RHE) (b).
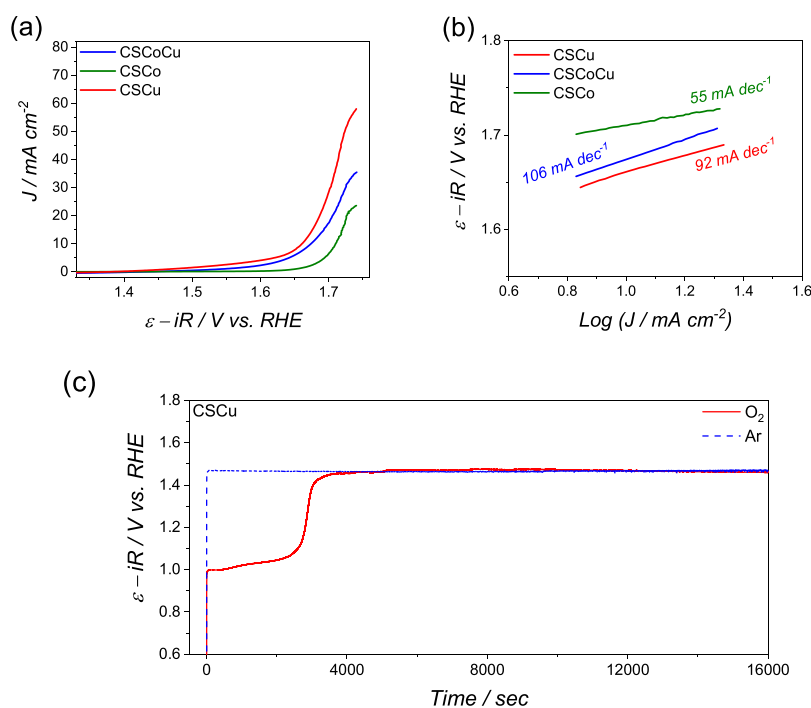

Figure 8. Specific OER activity of the perovskites (1 M KOH, 3000 rpm, Ar-saturated solution) (a), Tafel plots (b), and galvanostatic measurements for CSCu in O_2- and Ar-saturated electrolytes (1 M KOH, no rotation) (c).

the O_2/H_2O couple, plays a vital role in a fuel cell by excluding the formation of H_2O_2 via the $2e^-$ reduction mechanism. The higher activity of CSCoCu is owing to the higher Fermi levels, which makes O_2 reduction more favorable. EIS measurements (Figure 7b) indicate the improved charge transfer kinetics at the surface of CSCoCu compared to CSCo, while CSCu shows the slowest charge transfer at the surface/electrolyte interface. The energy difference (E_{diff}) between VBM and E_F is attributed to the valence orbital level, which is the active site in ORR. The higher E_F indicates a stronger adsorption of oxygen at the surface of the catalyst, which can result in an improved ORR activity.[32,33] Herein, CSCoCu with the highest E_F shows the highest ORR activity, while CSCu (lower E_F) demonstrates the lowest ORR activity (Figure 6). The fitted EIS plots are depicted in Figure S4, showing a perfect match with the R(C(R(Q(R(QR))))) EIS model. The equivalent circuits are also shown. The resistance at the electrolyte/electrode interface is the smallest for CSCoCu and the largest for CSCu. Moreover, the charge transfer at the bulk is hindered dramatically for CSCo and CSCu, while the increased ratio of

Co^{4+}/Co^{3+} in CSCoCu has a positive influence on the charge mobility in the bulk.

3.5.2. Oxygen Evolution Reaction. To omit the impact of surface area on the total activity of the synthesized perovskites, the specific activity was calculated taking into account the Brunauer–Emmett–Teller (BET) surface area and the space group of the perovskites (*cf*. Table S1). The specific OER activity of the catalysts, which is normalized by the specific surface area, is shown in Figure 8a. The onset potentials and the activity follow the difference between the potential of VBM and the potential of water splitting. In this context, CSCu shows a higher OER efficiency compared to both cobalt-containing perovskites, while CSCoCu is more active than CSCo. The electron affinity of B-sites is one of the descriptors in achieving lower onset potentials for water splitting;[34] copper (118.4 kJ mol^{-1}) has a higher electron affinity compared to cobalt (63.7 kJ mol^{-1}), which can lead to an enhanced polarization of water at copper compared to cobalt. This trend can be seen in the reported perovskites. Alternatively, another major descriptor of the OER activity is the occupation of e_g orbitals. The higher activity of copper-
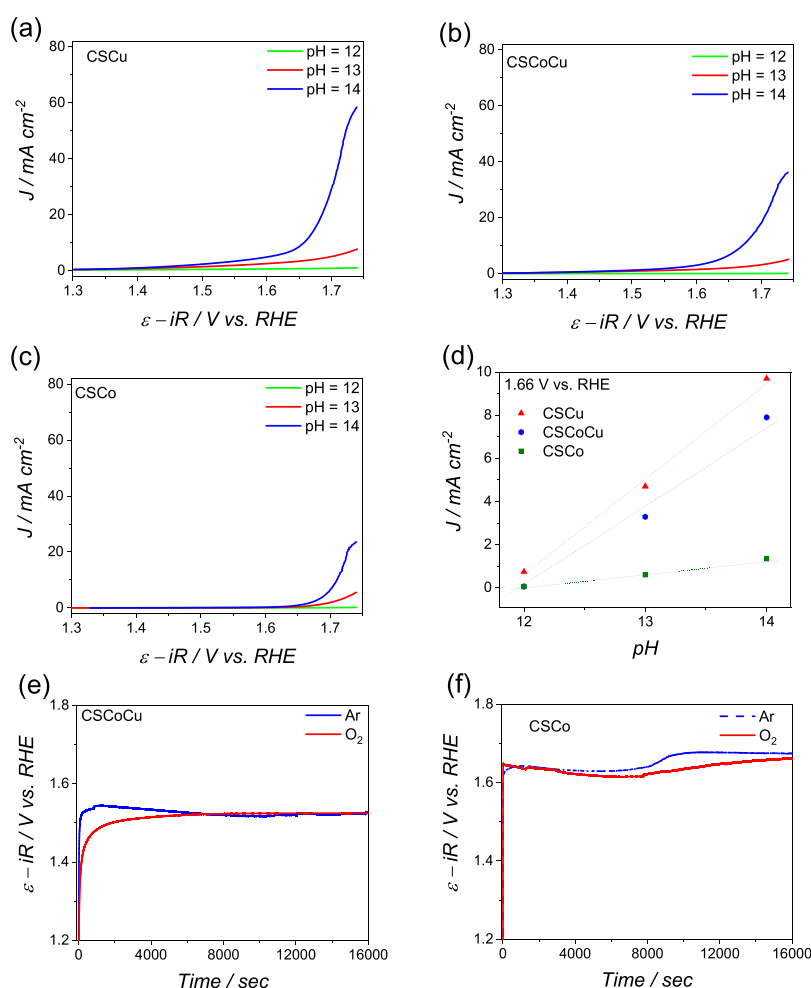
Figure 9. OER data from the electrodes: specific pH dependency for CSCu (a), CSCoCu (b), CSCu (c), surface area normalized at 1.66 V *vs* RHE (d), galvanostatic oxidation of CSCoCu (e), and CSCo (f) measurements employing RRDE for OER (3000 rpm), while no rotation was applied for galvanostatic oxidations.

Scheme 1. Mechanistic Pathways of OER for the Conventional (CM; (a)) and the Lattice Oxygen (LOM; (b)) Mechanisms[a14,33]
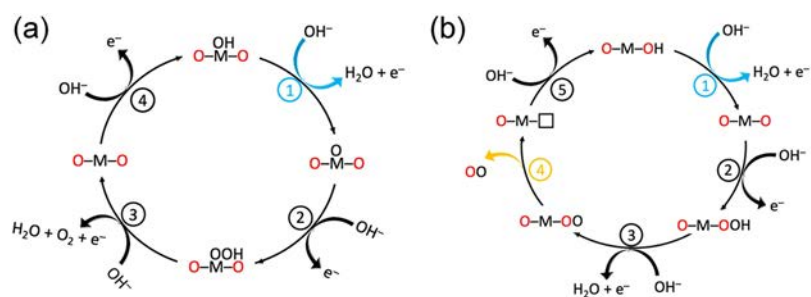
[a]The red-colored oxygen atoms originate from the lattice.[14,33]

based perovskites correlates with Henry Taube's theorem, in which the occupied e_g orbitals in Cu^{2+} (d^9), compared to the empty e_g orbitals in low-spin Co^{3+} (d^6) and Co^{4+} (d^5), make it kinetically active toward oxidation of water. This reasoning was also applied by Shao-Horn et al. for ABO_3 perovskites.[35] Although the activity of CSCo is lower than the copper-containing perovskites, based on the Tafel plots (Figure 8b), CSCo (55 mV dec^{-1}) offers improved kinetics at higher potentials compared to CSCu (92 mV dec^{-1}) and CSCoCu (106 mV dec^{-1}). In other words, the presence of Cu^{2+} and

Co^{4+} drives different kinetics of water oxidation at high potentials compared to CSCo. The shift of the onset potential of CSCoCu compared to CSCo due to the increased Co^{4+}/Co^{3+} ratio correlates with a previous report.[16]

3.5.3. Mechanism. The specific pH-dependent activity on the RHE scale is observed for CSCo, CSCoCu, and CSCu, which is shown in Figure 9a−d (currents were normalized at 1.66 V *vs* RHE). The two plausible OER mechanisms are (i) the conventional mechanism (CM; Scheme 1a) and (ii) the lattice oxygen mechanism (LOM; Scheme 1b).[15] In the first

one, surface (adsorbed) −OH groups are involved, while in the second one, the lattice oxygen is engaged. Another difference in these two mechanisms is related to the molecular oxygen release step: in CM, it is a one-step process (3) encompassing the removal of the −OOH group, while in LOM it consists of two consecutive processes involving the dehydrogenation reaction (3) and O_2 release (4). In oxides with a strong covalent B−O bond (B = Co and Cu), the kinetics of OER depends on the dehydrogenation of the surface hydroxyl groups. As discussed earlier, the electron affinity of copper in the reported perovskites is *ca.* twice higher than that of cobalt. Therefore, dehydrogenation of the surface containing copper will be far more efficient compared to the situation with cobalt. This phenomenon is consistent with the shift of the VBM to more positive energies. Herein, the presence of Cu^{2+} induces a shift of the valence band maximum to a lower energy.

Shi et al. suggest that the increased OER activity in strongly basic media favors the lattice oxygen mechanism.[36] The enhancement of OER activity in the case of CSCu is supported by galvanostatic measurements (Figure 8c). The plausible route for the galvanostatic oxidation of the ABO_3 perovskite is as follows:[37] $ABO_{3-\delta} + 2\delta OH^- \rightarrow ABO_3 + \delta H_2O + 2\delta e^-$. The progress of this reaction depends on the redox properties of the material but not on the presence of molecular oxygen in the system.[14] In this context, during the galvanostatic charging of CSCu in the presence of O_2, oxygen intercalation is observed, which is not the case in argon (Figure 8c). In other words, in O_2-saturated electrolytes, the lattice in CSCu is filled by O_2 instead of OH^-. This phenomenon delivers the faster kinetics observed in oxygen-saturated media due to the formation of an O−Cu−**O**OH intermediate instead of O−Cu−**O**H. We did not observe an oxygen intercalation effect either for CSCoCu (Figure 9e) or for CSCo (Figure 9f). In the same context, $SrCoO_3$ is known for intercalation of oxygen during galvanostatic oxidation;[14] however, it has been shown that substituting Sr^{2+} with Ca^{2+} makes O_2 intercalation difficult, which stems from the higher electronegativity of Ca^{2+} compared to Sr^{2+} and hence weakening the B−O bond (B = Co and Cu).[34,38] This phenomenon will lead to a lower polarization of the Co-containing surface, while a higher electron affinity of copper outweighs the Ca^{2+} effect, enabling O_2 intercalation to the lattice of CSCu, which shows a good correlation with the potential difference between the H_2O/H_2 redox couple and the Fermi level of the material (Figure 5). Figure 8c shows that $\varepsilon - iR$ reaches the first plateau (attributed to the intercalation of O_2) at around 1 V *vs* RHE before reaching the OER's onset potential higher than 1.4 V. Noteworthy, in the Ar-saturated electrolytes, the occupation of the active site involves OH^-.

4. CONCLUSIONS

In summary, UPS and KP measurements confirm the decreased work function in Co-containing perovskites under vacuum, which is reflected in the increased energy of the Fermi level. However, the KP measurements under ambient conditions reveal the increased work function, which results from the interactions between the surface of the perovskites and adsorbates. CSCu shows the lowest onset potential of OER and the highest activity, which is mainly a consequence of the lower energy of VBM and the smaller difference between the Fermi level and the VBM (top of O 2p) orbital. For CSCu, VBM and E_F are characterized by more positive potentials compared to the Co-containing perovskites. The increased

content of Co^{4+} in CSCoCu improves the adsorption of water, and OH groups shift the E_F to lower energies, increasing the ORR activity/selectivity of CSCoCu compared to both CSCo and CSCu. Likewise, the Fermi level of CSCo is decreased due to the adsorption of water and OH groups, which resulted in an improved ORR activity compared to CSCu. The superiority of CSCu in OER compared to Co-containing perovskites is directly related to the more positive potentials of VBM, which results in a higher energy difference between VBM and the H_2O/O_2 redox couple, facilitating water oxidation. This finding is in direct correlation with Yamada et al.'s report about the influence of the charge energy difference on the OER activity of perovskites.[39] As shown by Varignon et al.,[30] the VBM of perovskites is O 2p orbitals; therefore, the position of the VBM plays a crucial role in increasing the activity of perovskites in OER. In summary, in this study, the difference in energy between the Fermi level and VBM plays an insignificant role in OER, while it plays a significant role in the ORR activity of the perovskites. However, herein, the governing factor in the OER activity difference between the perovskites stems from the VBM position. The larger the difference between the energies of VBM and water, the stronger the adsorption. This phenomenon allows the formation of a stronger covalent bond with water and OH, leading to the higher efficiency of CSCu in OER. Therefore, to elucidate the mechanism of OER/ORR, it is necessary to consider the adsorbates' impact on the Fermi levels, which can increase/decrease the Fermi level.

■ ASSOCIATED CONTENT

Ⓢ Supporting Information

The Supporting Information is available free of charge at https://pubs.acs.org/doi/10.1021/acsaenm.3c00288.

> Characterization results on XRD and figures related to the ORR activity of electrodes obtained from RRDE experiments (PDF)

■ AUTHOR INFORMATION

Corresponding Authors

Taymaz Tabari − *Faculty of Chemistry, Jagiellonian University, 30-387 Kraków, Poland;* ⊙ orcid.org/0000-0003-3999-5001; Email: taymaz.tabari@uj.edu.pl

Wojciech Macyk − *Faculty of Chemistry, Jagiellonian University, 30-387 Kraków, Poland;* ⊙ orcid.org/0000-0002-1317-6115; Email: macyk@chemia.uj.edu.pl

Authors

Marcin Kobielusz − *Faculty of Chemistry, Jagiellonian University, 30-387 Kraków, Poland;* ⊙ orcid.org/0000-0003-2707-0415

Dheerendra Singh − *Department of Chemical Engineering, Indian Institute of Technology Bombay, Mumbai 400076, India*

Jiaguo Yu − *Laboratory of Solar Fuel, Faculty of Materials Science and Chemistry, China University of Geosciences, Wuhan 430074, P. R. China;* ⊙ orcid.org/0000-0002-0612-8633

Complete contact information is available at:
https://pubs.acs.org/10.1021/acsaenm.3c00288

Notes

The authors declare no competing financial interest.

■ REFERENCES

(1) (a) Keller, N.; Ivanez, J.; Highfield, J.; Ruppert, A. M. Photo-/thermal synergies in heterogeneous catalysis: towards low-temperature (solar-driven) processing for sustainable energy and chemicals. *Appl. Catal., B* **2021**, *296*, No. 120320. (b) Zhou, P.; Chen, H.; Chao, Y.; Zhang, Q.; Zhang, W.; Lv, F.; Gu, L.; Zhao, Q.; Wang, N.; Wang, J.; Guo, S. Single-atom Pt-I3 sites on all-inorganic Cs2ₛnI6 perovskite for efficient photocatalytic hydrogen production. *Nat. Commun.* **2021**, *12*, No. 4412. (c) Qin, C.; Sandanayaka, A. S.; Zhao, C.; Matsushima, T.; Zhang, D.; Fujihara, T.; Adachi, C. Stable room-temperature continuous-wave lasing in quasi-2D perovskite films. *Nature* **2020**, *585*, 53−57. (d) Meng, Q.; Yan, J.; Wu, R.; Liu, H.; Sun, Y.; Wu, N.; Xiang, J.; Zheng, L.; Zheng, J.; Han, B. Sustainable production of benzene from lignin. *Nat. Commun.* **2021**, *12*, No. 4534.

(2) (a) Suryanto, B. H. R.; Wang, Y.; Hocking, R. K.; Adamson, W.; Zhao, C. Overall electrochemical splitting of water at the heterogeneous interface of nickel and iron oxide. *Nat. Commun.* **2019**, *10*, No. 5599. (b) Shi, H.; Zhou, Y.-T.; Yao, R.-Q.; Wan, W.-B.; Ge, X.; Zhang, W.; Wen, Z.; Lang, X.-Y.; Zheng, W.-T.; Jiang, Q. Spontaneously separated intermetallic Co3$_M$O from nanoporous copper as versatile electrocatalysts for highly efficient water splitting. *Nat. Commun.* **2020**, *11*, No. 2940. (c) Chinnadurai, D.; Rajendiran, R.; Li, O. L.; Prabakar, K. Mn-Co bimetallic phosphate on electrodeposited PANI nanowires with composition modulated structural morphology for efficient electrocatalytic water splitting. *Appl. Catal., B* **2021**, *292*, No. 120202.

(3) (a) Ioroi, T.; Siroma, Z.; Yamazaki, Si.; Yasuda, K. Electro-catalysts for PEM fuel cells. *Adv. Energy Mater.* **2019**, *9*, No. 1801284. (b) Qi, M.; Zeng, Y.; Hou, M.; Gou, Y.; Song, W.; Chen, H.; Wu, G.; Jia, Z.; Gao, Y.; Zhang, H.; Shao, Z. Free-standing and Ionomer-free 3D Platinum Nanotrough Fiber Network Electrode for Proton Exchange Membrane Fuel Cells. *Appl. Catal., B* **2021**, *298*, No. 120504. (c) Qu, X.; Han, Y.; Chen, Y.; Lin, J.; Li, G.; Yang, J.; Jiang, Y.; Sun, S. Stepwise pyrolysis treatment as an efficient strategy to enhance the stability performance of Fe-NX/$_C$ electrocatalyst towards oxygen reduction reaction and proton exchange membrane fuel cell. *Appl. Catal., B* **2021**, *295*, No. 120311.

(4) Li, Y.; Dai, H. Recent advances in zinc−air batteries. *Chem. Soc. Rev.* **2014**, *43*, 5257−5275.

(5) Lv, L.; He, X.; Wang, J.; Ruan, Y.; Ouyang, S.; Yuan, H.; Zhang, T. Charge localization to optimize reactant adsorption on KCu7S4/CuO interfacial structure toward selective CO$_2$ electroreduction. *Appl. Catal., B* **2021**, *298*, No. 120531.

(6) Guo, S.; Sun, S. FePt nanoparticles assembled on graphene as enhanced catalyst for oxygen reduction reaction. *J. Am. Chem. Soc.* **2012**, *134*, 2492−2495.

(7) Feng, Y.-Y.; Si, S.; Deng, G.; Xu, Z.-X.; Pu, Z.; Hu, H.-S.; Wang, C.-B. Copper-doped ruthenium oxide as highly efficient electro-catalysts for the evolution of oxygen in acidic media. *J. Alloys Compd.* **2022**, *892*, No. 162113.

(8) Cuong, H. N.; Pansambal, S.; Ghotekar, S.; Oza, R.; Hai, N. T. T.; Viet, N. M.; Nguyen, V.-H. New frontiers in the plant extract mediated biosynthesis of copper oxide (CuO) nanoparticles and their potential applications: A review. *Environ. Res.* **2022**, *203*, No. 111858.

(9) (a) Tan, P.; Liu, M.; Shao, Z.; Ni, M. Recent advances in perovskite oxides as electrode materials for nonaqueous lithium−oxygen batteries. *Adv. Energy Mater.* **2017**, *7*, No. 1602674. (b) Zhu, Y.; Zhou, W.; Shao, Z. Perovskite/carbon composites: applications in oxygen electrocatalysis. *Small* **2017**, *13*, No. 1603793.

(10) Chen, H.; Motuzas, J.; Martens, W.; da Costa, J. C. D. Degradation of azo dye Orange II under dark ambient conditions by calcium strontium copper perovskite. *Appl. Catal., B* **2018**, *221*, 691−700.

(11) Xie, L.; Liu, X.; Chang, J.; Zhang, C.; Li, Y.; Zhang, H.; Zhan, S.; Hu, W. Enhanced redox activity and oxygen vacancies of perovskite triggered by copper incorporation for the improvement of electro-Fenton activity. *Chem. Eng. J.* **2022**, *428*, No. 131352.

(12) Pan, K.; Yang, C.; Hu, J.; Yang, W.; Liu, B.; Yang, J.; Liang, S.; Xiao, K.; Hou, H. Oxygen vacancy mediated surface charge redistribution of Cu-substituted LaFeO3 for degradation of bisphenol A by efficient decomposition of H$_2$O$_2$. *J. Hazard. Mater.* **2020**, *389*, No. 122072.

(13) Mefford, J. T.; Rong, X.; Abakumov, A. M.; Hardin, W. G.; Dai, S.; Kolpak, A. M.; Johnston, K. P.; Stevenson, K. J. Water electrolysis on La$_{1−x}$Sr$_x$CoO$_{3−δ}$ perovskite electrocatalysts. *Nat. Commun.* **2016**, *7*, No. 11053.

(14) Grimaud, A.; Diaz-Morales, O.; Han, B.; Hong, W. T.; Lee, Y.-L.; Giordano, L.; Stoerzinger, K. A.; Koper, M. T.; Shao-Horn, Y. Activating lattice oxygen redox reactions in metal oxides to catalyse oxygen evolution. *Nat. Chem.* **2017**, *9*, 457−465.

(15) Pan, Y.; Xu, X.; Zhong, Y.; Ge, L.; Chen, Y.; Veder, J.-P. M.; Guan, D.; O'Hayre, R.; Li, M.; Wang, G.; et al. Direct evidence of boosted oxygen evolution over perovskite by enhanced lattice oxygen participation. *Nat. Commun.* **2020**, *11*, No. 2002.

(16) Li, X.; Wang, H.; Cui, Z.; Li, Y.; Xin, S.; Zhou, J.; Long, Y.; Jin, C.; Goodenough, J. B. Exceptional oxygen evolution reactivities on CaCoO3 and SrCoO3. *Sci. Adv.* **2019**, *S*, No. eaav6262.

(17) Singh, D.; Tabari, T.; Ebadi, M.; Trochowski, M.; Yagci, M. B.; Macyk, W. Efficient synthesis of BiFeO3 by the microwave-assisted sol-gel method:"A" site influence on the photoelectrochemical activity of perovskites. *Appl. Surf. Sci.* **2019**, *471*, 1017−1027.

(18) Chen, R.; Yang, C.; Cai, W.; Wang, H.-Y.; Miao, J.; Zhang, L.; Chen, S.; Liu, B. Use of platinum as the counter electrode to study the activity of nonprecious metal catalysts for the hydrogen evolution reaction. *ACS Energy Lett.* **2017**, *2*, 1070−1075.

(19) (a) Puri, N.; Tandon, R. P.; Mahapatro, A. K. Fully dense hot pressed calcium cobalt oxide ceramics. *Ceram. Int.* **2018**, *44*, 6337−6342. (b) Panchakarla, L. S.; Lajaunie, L.; Ramasubramaniam, A.; Arenal, R.; Tenne, R. Strontium cobalt oxide misfit nanotubes. *Chem. Mater.* **2016**, *28*, 9150−9157.

(20) (a) Wang, J.; Yang, T.; Lei, L.; Huang, K. Ta-Doped SrCoO$_{3−δ}$ as a promising bifunctional oxygen electrode for reversible solid oxide fuel cells: a focused study on stability. *J. Mater. Chem. A* **2017**, *S*, 8989−9002. (b) Dung, D. D.; Hung, N. T. Magnetic properties of (1− x)Bi$_{0.5}$Na$_{0.5}$TiO$_3$ + xSrCoO$_{3−δ}$ solid-solution materials. *Appl. Phys. A: Mater. Sci. Process.* **2020**, *126*, No. 240.

(21) Li, Z.; Chen, X.; Chen, Y.; Zhang, Q.; Zhang, H.; Zhang, J.; Shi, W.; He, B.; Zhang, J.; Song, J.; et al. Infinite-layer/perovskite oxide heterostructure-induced high-spin states in SrCuO 2/SrRuO 3 bilayer films. *Mater. Horiz.* **2021**, *8*, 3468−3476.

(22) Tabari, T.; Kobielusz, M.; Duch, J.; Singh, D.; Kotarba, A.; Macyk, W. Design, engineering, and performance of nanorod-Fe2O3@rGO@LaSrFe2-nConO6 (n = 0, 1) composite architectures: the role of double oxide perovskites in reaching high solar to hydrogen efficiency. *Appl. Catal., B* **2020**, *272*, No. 118952.

(23) Butt, S.; Xu, W.; He, W. Q.; Tan, Q.; Ren, G. K.; Lin, Y.; Nan, C.-W. Enhancement of thermoelectric performance in Cd-doped Ca$_3$Co$_4$O$_9$ via spin entropy, defect chemistry and phonon scattering. *J. Mater. Chem. A* **2014**, *2*, 19479−19487.

(24) Cai, Z.; Kubicek, M.; Fleig, J.; Yildiz, B. Chemical Heterogeneities on La$_{0.6}$Sr$_{0.4}$CoO$_{3−δ}$ Thin Films- Correlations to Cathode Surface Activity and Stability. *Chem. Mater.* **2012**, *24*, 1116−1127.

(25) Keswani, B.; Devan, R.; Kambale, R.; James, A.; Manandhar, S.; Kolekar, Y.; Ramana, C. Correlation between structural, magnetic and ferroelectric properties of Fe-doped (Ba-Ca) TiO_3 lead-free piezo-electric. *J. Alloys Compd.* **2017**, *712*, 320−333.

(26) Jain, S.; Shah, J.; Negi, N. S.; Sharma, C.; Kotnala, R. K. Significance of interface barrier at electrode of hematite hydroelectric cell for generating ecopower by water splitting. *Int. J. Energy Res.* **2019**, *43*, 4743−4755.

(27) Zhu, Z.; Shi, Y.; Aruta, C.; Yang, N. Improving electronic conductivity and oxygen reduction activity in Sr-doped lanthanum cobaltite thin films: Cobalt valence state and electronic band structure effects. *ACS Appl. Energy Mater.* **2018**, *1*, 5308−5317.

(28) Tabari, T.; Kobielusz, M.; Jarosz-Duda, A.; Singh, D.; Kotarba, A.; Błachowski, A.; Yu, J.; Macyk, W. Photoelectrochemical activity of visible light-responsive $BiVO_4@$ $La_{1-x}Sr_xFeO_{3-\delta}$ (x = 0, 0.2, 0.4) heterojunction architectures−optimizing activity by tuning Fe−O bond in perovskites. *Appl. Surf. Sci.* **2023**, *616*, No. 156513.

(29) Kim, S.; Ji, S.; Kim, K. H.; Roh, S. H.; Cho, Y.; Lee, C.-L.; Lee, K.-S.; Choi, D.-G.; Choi, H.; Kim, J. K.; Park, J. H. Revisiting surface chemistry in TiO_2: A critical role of ionic passivation for pH-independent and anti-corrosive photoelectrochemical water oxidation. *Chem. Eng. J.* **2021**, *407*, No. 126929.

(30) Varignon, J.; Bibes, M.; Zunger, A. Origin of band gaps in 3d perovskite oxides. *Nat. Commun.* **2019**, *10*, No. 1658.

(31) Park, J.; Wu, Y.-N.; Saidi, W. A.; Chorpening, B.; Duan, Y. First-principles exploration of oxygen vacancy impact on electronic and optical properties of $ABO_{3-\delta}$ (A = La, Sr; B = Cr, Mn) perovskites. *Phys. Chem. Chem. Phys.* **2020**, *22*, 27163−27172.

(32) (a) Del Cueto, M.; Ocón, P.; Poyato, J. Comparative study of oxygen reduction reaction mechanism on nitrogen-, phosphorus-, and boron-doped graphene surfaces for fuel cell applications. *J. Phys. Chem. C* **2015**, *119*, 2004−2009. (b) Zhao, Z.; Li, M.; Zhang, L.; Dai, L.; Xia, Z. Design principles for heteroatom-doped carbon nanomaterials as highly efficient catalysts for fuel cells and metal−air batteries. *Adv. Mater.* **2015**, *27*, 6834−6840.

(33) Jiao, Y.; Zheng, Y.; Jaroniec, M.; Qiao, S. Z. Origin of the electrocatalytic oxygen reduction activity of graphene-based catalysts: a roadmap to achieve the best performance. *J. Am. Chem. Soc.* **2014**, *136*, 4394−4403.

(34) Kuznetsov, D. A.; Han, B.; Yu, Y.; Rao, R. R.; Hwang, J.; Román-Leshkov, Y.; Shao-Horn, Y. Tuning redox transitions via inductive effect in metal oxides and complexes, and implications in oxygen electrocatalysis. *Joule* **2018**, *2*, 225−244.

(35) Suntivich, J.; May, K. J.; Gasteiger, H. A.; Goodenough, J. B.; Shao-Horn, Y. A perovskite oxide optimized for oxygen evolution catalysis from molecular orbital principles. *Science* **2011**, *334*, 1383−1385.

(36) (a) Shi, Y.; Xie, R.; Liu, X.; Zhang, N.; Aruta, C.; Yang, N. Tunable pH-dependent oxygen evolution activity of strontium cobaltite thin films for electrochemical water splitting. *Phys. Chem. Chem. Phys.* **2019**, *21*, 16230−16239. (b) Yang, C.; Batuk, M.; Jacquet, Q.; Rousse, G.; Yin, W.; Zhang, L.; Hadermann, J.; Abakumov, A. M.; Cibin, G.; Chadwick, A.; et al. Revealing pH-dependent activities and surface instabilities for Ni-based electrocatalysts during the oxygen evolution reaction. *ACS Energy Lett.* **2018**, *3*, 2884−2890.

(37) Mefford, J. T.; Hardin, W. G.; Dai, S.; Johnston, K. P.; Stevenson, K. J. Anion charge storage through oxygen intercalation in $LaMnO_3$ perovskite pseudocapacitor electrodes. *Nat. Mater.* **2014**, *13*, 726−732.

(38) Han, B.; Grimaud, A.; Giordano, L.; Hong, W. T.; Diaz-Morales, O.; Yueh-Lin, L.; Hwang, J.; Charles, N.; Stoerzinger, K. A.; Yang, W.; et al. Iron-based perovskites for catalyzing oxygen evolution reaction. *J. Phys. Chem. C* **2018**, *122*, 8445−8454.

(39) Yamada, I.; Takamatsu, A.; Asai, K.; Shirakawa, T.; Ohzuku, H.; Seno, A.; Uchimura, T.; Fujii, H.; Kawaguchi, S.; Wada, K.; et al. Systematic study of descriptors for oxygen evolution reaction catalysis in perovskite oxides. *J. Phys. Chem. C* **2018**, *122*, 27885−27892.